

Although some uncertainties exist about these climatic responses (23), the medium-high scenario commonly forms the basis of current attempts to predict the impact of climate change on human health. Outputs of the medium-high scenario are the average of four separate GCM runs and are given as differences between the modeled present and modeled future conditions; the high-scenario outputs are scaled versions of the medium-high outputs (23). Following usual practice, the GCM differences were added to the observed 30-year climatic means (after cubic-spline interpolation to the same spatial resolution), to generate the predicted future climate surfaces that were used in the present analysis.

20. The "Gridded Population of the World" unsmoothed population density data file created by the Socioeconomic Data and Applications Center at Columbia University (Palisades, NY) was obtained from the Center for

International Earth Science Information Network at ftp://ftp.ciesin.org/pub/data/Grid_Pop_World. This record of the 1994 human population density per square kilometer was turned into a raster image at 1/12° spatial resolution and was subsequently used to estimate the total human population within the malarious areas shown in Fig. 1, A through C, allowing for the different land areas corresponding to pixels at different latitudes. Land pixels in the malaria map imagery were mapped onto their equivalent 6 by 6 grid in the population density imagery, from which population totals were extracted and summed. This method estimated a total global population of 5611 million people in 1994, of which 2727 million lived within the predicted malarious areas of Fig. 1A. Under the medium-high scenario, 357 million people live within areas that are currently malaria-free but are predicted to become malarious by 2050, and 334

million live within currently malarious areas that are predicted to become unsuitable by 2050, a net increase of 23 million, or +0.84% on the 1994 baseline population data. For the high scenario, the corresponding figures are 389 million, 414 million, and a net decrease of 25 million or -0.92%, respectively (Fig. 1C).

21. Z. K. Ma and R. L. Redmond, *Photogramm. Eng. Remote Sensing* **61**, 435 (1995).
22. D. J. Rogers, S. I. Hay, M. J. Packer, *Ann. Trop. Med. Parasitol.* **90**, 225 (1996).
23. M. Hulme and G. J. Jenkins, "Climate change scenarios for the UK: Scientific report" (Climatic Research Unit, Norwich, UK, 1998).
24. We thank the Department for International Development (grant R6626 to D.J.R.) and the Wellcome Trust (S.E.R.) for financial support and G. B. White and S. I. Hay for helpful comments.

31 March 2000; accepted 22 June 2000

Cholera Dynamics and El Niño–Southern Oscillation

Mercedes Pascual,^{1*} Xavier Rodó,² Stephen P. Ellner,³ Rita Colwell,⁴ Menno J. Bouma⁵

Analysis of a monthly 18-year cholera time series from Bangladesh shows that the temporal variability of cholera exhibits an interannual component at the dominant frequency of El Niño–Southern Oscillation (ENSO). Results from nonlinear time series analysis support a role for both ENSO and previous disease levels in the dynamics of cholera. Cholera patterns are linked to the previously described changes in the atmospheric circulation of south Asia and, consistent with these changes, to regional temperature anomalies.

Cholera remains a major public health problem in many areas of the world, including Bangladesh and India. A climate influence on cholera has long been debated (1), and it has been suggested that ENSO, a major source of interannual climate variability, drives the interannual variation of the disease (2, 3). For example, cholera reappeared in Peru with the El Niño event of 1991–92 and seems to fluctuate seasonally in Bangladesh with sea surface temperature (SST) in the Bay of Bengal (2, 4). Recent studies of time series for diarrhoeal diseases in Peruvian children have shown an increase in cases associated with warmer temperatures and the 1997–98 El Niño (5, 6). *Vibrio cholerae*, the

bacterium that causes the disease, is now known to inhabit brackish waters and estuarine systems (2) and thus might be sensitive to climate patterns. Here we examine the associations between cholera and ENSO and between cholera and climate at interannual time scales, using an 18-year record from Bangladesh where the disease is endemic. A nonlinear time series approach allows us to consider different hypotheses for the roles of environmental driving variables and the inherent disease dynamics in producing the interannual variability of cholera.

The disease data consist of a monthly time series for cholera incidence between January 1980 and March 1998 in Dhaka, Bangladesh (Fig. 1A). Over the same time span, the monthly SST anomaly in a region of the equatorial Pacific provides an index for ENSO (Fig. 1B). The cholera time series displays the well-known seasonal variation of the disease—typically described as bimodal, with a small peak in the spring and a larger one in the fall or early winter—but also shows a multiyear modulation of the seasonal cycles. The interannual variability of cholera cases has a dominant frequency of 1/3.7 years, as shown by singular spectrum analysis (7, 8) (Fig. 2). The same dominant frequency is found for the ENSO time series, which suggests that climate variability acts as a driver in the dynamics of the disease (Fig. 2). Alternatively, however, this low-frequency variability could arise solely from the seasonal

forcing of disease transmission (9). To investigate the role of ENSO in light of this alternative explanation, we consider a nonlinear time series approach that allows us to compare specific alternative hypotheses for the underlying factors in cholera dynamics. Because the null (non-ENSO) hypothesis is a nonlinear interaction between seasonality and cholera dynamics, the use of standard linear time series models would strongly bias the comparison in favor of the ENSO alternative.

Lacking information that could be used to specify a valid mechanistic model for the ENSO effect, we use time series models that are both nonlinear and nonparametric and are effective at modeling high-dimensional relationships. The dynamics of a variable of interest, N_t , a measure of cholera levels, are modeled with a nonlinear equation of the form

$$N_{t+T_p} = f\left(N_t, N_{t-\tau}, N_{t-2\tau}, \dots, N_{t-(d-1)\tau}, \sin\frac{2\pi}{12}t, \cos\frac{2\pi}{12}t, E_{t-\tau_j}\right) + e_t \quad (1)$$

where T_p is a prediction time, f is a nonlinear function, and E_t is the environmental forcing under consideration (10, 11). The sin and cos functions implement a seasonal clock and e_t represents the IID random noise variables. The parameters τ , τ_j , and d denote, respectively, two different time lags and the number of time delay variables. Time delay coordinates are used in the model as surrogates for unobserved variables influencing the endogenous dynamics of the disease, such as the fraction of susceptible individuals in the population (12, 13). The functional form of f is not specified in a rigid form. Instead, the shape of f is determined by the data, using an objective model selection criterion: generalized cross-validation (GCV) (14). We used the GCV criterion to compare models with and without seasonality and with and without the environmental covariate E_t (Table 1). The selected model is low-dimensional and incorporates both seasonality and ENSO as external forcings (Fig. 3). The model

¹Center of Marine Biotechnology, University of Maryland Biotechnology Institute, 701 East Pratt Street, Suite 236, Columbus Center, Baltimore, MD 21202, USA, and Biology Department, Woods Hole Oceanographic Institution, Woods Hole, MA 02543, USA.

²Climate Research Group, PCB—University of Barcelona, and Department of Ecology, University of Barcelona, 08028 Barcelona, Catalunya, Spain. ³Department of Ecology and Evolutionary Biology, Cornell University, Ithaca, NY 14853, USA. ⁴Center of Marine Biotechnology, University of Maryland Biotechnology Institute, Baltimore, MD 21202, USA, and Department of Cell and Molecular Biology, University of Maryland, College Park, College Park, MD 20742, USA. ⁵Department of Infectious and Tropical Diseases, London School of Hygiene and Tropical Medicine, University of London, London WC1E 7HT, UK.

*To whom correspondence should be addressed. E-mail: mercedes@pampero.umbi.umd.edu

REPORTS

also accounts for the largest fraction of the variance in the data.

Could the better fit (the higher r^2) of the model incorporating ENSO simply result from the larger number of variables and parameters in that model? To address this question, we conducted parametric bootstrap tests for the significance of the improvement in fit (15). The result of these comparisons (Table 2) shows that the addition of the ENSO index as a predictor variable is highly significant. But so is the addition of previous disease levels. These results support a role for both extrinsic factors (ENSO and seasonality) and intrinsic ones (previous disease levels) in the dynamics of cholera.

A positive influence of previous disease levels indicates a density-dependent effect in cholera transmission. In the fall, when the largest values generally occur, this effect is of the

compensatory type: Cholera incidence increases monotonically with previous levels but with an ever decreasing slope. Compensatory density dependence can result from a decrease in the number of susceptibles in the population after a large number of cases and/or from the complex-

ities of transmission through water in the environment. Overcompensatory density dependence, a negative effect of previous levels on current levels, has been observed in other infectious diseases (16) but is not apparent here for a time lag of 2 months. Although we cannot

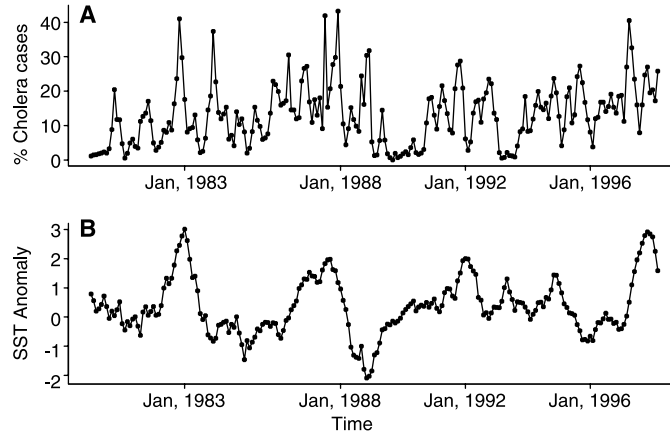


Fig. 1. (A) Time series of percentage of cholera cases obtained by the ICDDR,B (International Centre for Diarrhoeal Disease Research, Bangladesh, in Dhaka) from a systematic sample of the patients visiting the facility. (B) ENSO time series given by the index Niño 3.4.

Table 1. Comparison of models using the GCV model selection criterion V_c . The model (defined by Eqs. 1 and 2) is fitted to the cholera time series after the data are square-root-transformed, which normalizes the residuals and stabilizes the variance. A time lag t of 2 months is used, based on the well-known rule of thumb of choosing the lag for which the autocorrelation function first crosses 0.5. Thus, Eq. 1 takes the general form

$$Y_{t+2} = f\left(Y_t, Y_{t-2}, \dots, Y_{t-2+(d-1)}, \sin\frac{2\pi}{12}t, \cos\frac{2\pi}{12}t, E_{t-\tau_f}\right) + e_t \quad (4)$$

where $Y_t = \sqrt{N_t}$. When seasonality is incorporated but not the ENSO index, low-dimensional models ($d = 1$ and $d = 2$) are selected (that is, they have the smallest values of the cross-validation criterion V_c). The importance of seasonality is demonstrated by comparing these models to their autonomous counterparts. Models with an equivalent or larger number of independent variables (for example, $d = 4$ and $d = 6$) but no seasonality have larger values of V_c . The importance of ENSO is examined by incorporating the ENSO index into the simplest seasonal model ($d = 1$) at different time lags (τ_f , between 0 and 12 months). The smallest V_c value is obtained for the model with $\tau_f = 11$. This model is also selected over the seasonal one with an equal number of independent variables ($d = 2$). It has a higher r^2 value than the seasonal and autonomous models, accounting for a larger fraction of the variance. (For all models, the number of neurons k used in fitting the function f of Eq. 2 varied between 1 and 5. Only the model with the smallest V_c is reported here.) A value of k larger than one in the selected ENSO model indicates that a linear time series model is not adequate to fit the causal relationships and would give a less reliable conclusion about the role of ENSO.

Environmental covariate	Seasonal clock	d	k	GCV score V_c	r^2 (%)
-	+	1	2	0.937	55
-	+	2	2	0.932	57
-	-	4	3	1.259	51
-	-	6	3	1.176	60
E_{t-11}	+	1	3	0.819	67

Fig. 2. Singular spectrum analysis applied to the ENSO index and to the cholera time series with seasonality removed. For both time series, a window length of 60 months was used. The dominant eigenvalues for both data sets are given by a pair, indicating the existence of an underlying oscillatory component. The eigenspectrum of nonlinear signals typically exhibit three distinct regions: first, a group of significant eigenvalues, used here to obtain the reconstructed components (A); then an intermediate slope; and finally the noise floor. Error bars were calculated from the inverse of the lag-one AR coefficient with conservative weights according to (23, 24). Projections of the signal onto the empirical orthogonal functions (EOFs) of the corresponding eigenvalues give the different principal components (PCs). To reconstruct the time series corresponding to several EOFs, the associated PCs are combined. This reconstruction process preserves the phase of the time series. In addition, no information is lost in the reconstruction, because the sum of all the individual reconstructed components gives the original time series. Here the four first components were used, which explain 46 and 76% of the variance for the cholera and ENSO time series, respectively. In (B), spectra were computed with the maximum entropy method (MEM) applied to the reconstructed components in (A), respectively. The dominant peak in both spectra corresponds to a frequency of 0.0225 months (or 1/3.7 years). Results are robust to varying resolutions and MEM orders. Similar results were obtained with the multi-taper method (MTM). The peak corresponding to 0.0225 months was significant at a 99% level and proved robust to varying resolutions and tapers.

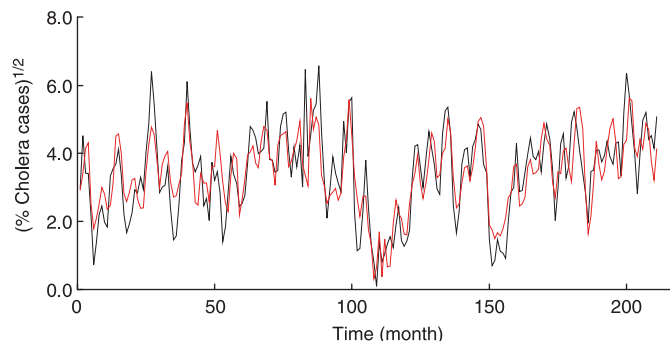
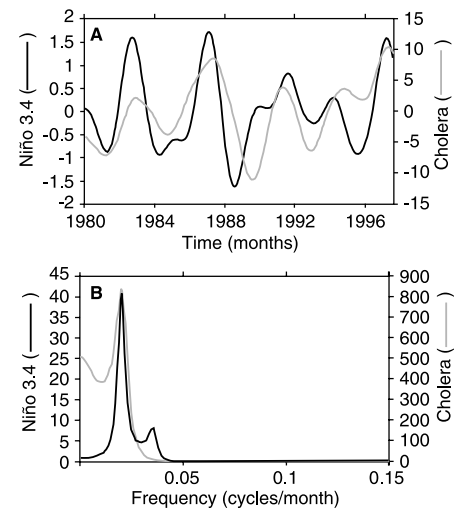


Fig. 3. The (square-root-transformed) cholera data (black line) and the 2-months-ahead prediction of the fitted model incorporating both seasonality and ENSO at a lag $\tau_f = 11$ (red line).

REPORTS

rule out overcompensation for disease levels higher than the ones observed, this difference can result from a less effective immunity in the case of cholera.

A positive effect of ENSO is observed on the 2-month-ahead predictions of cholera incidence in the fall (November, for example). This is the time of the year during which the second and largest outbreak of cholera typically occurs in the bimodal seasonal cycle. Cholera incidence 2 months ahead increases with both SST anomaly and present incidence. The sensitivity to changes in the ENSO index is largest for increasing negative values of the SST anomaly; that is, for changes that anticipate an El Niño, and for increasing and large positive values—changes that occur during an El Niño. Later in the spring (April, for example), the levels of cholera incidence are typically lower. Disease levels can either increase or decrease with the ENSO index. Incidence goes up with increasing negative values of the SST anomaly, as for changes that would anticipate an El Niño. It decreases, however, with increasing positive values of the SST anomaly. One possible interpretation of this pattern is that large peaks in the fall are typically followed by small increases of

incidence in the spring (from February into April). This inverse relation is indeed observed in the data. These results indicate that the dynamics of cholera in Bangladesh are consistent with a remote forcing by ENSO.

ENSO is thought to affect the atmospheric circulation in the Indian Ocean and south Asia: Changes in cloud cover and evaporation associated with a weakening of the local Hadley cell increase the heat flux entering this region a few months after warming of the Pacific during an El Niño (17). This provides a possible mechanistic connection between El Niño and regional climate variables potentially having an impact on cholera in Bangladesh. We considered three interrelated climate variables: upper-tropospheric humidity, cloud cover, and top-of-atmosphere absorbed solar radiation. From global satellite-retrieved fields for these variables (18–20), we computed global correlation maps between the cholera time series in Dhaka and the climate time series at the different points of the global grid, with temporal lags ranging from ±12 months. The strongest associations are

found for negative lags; that is, for the climate variables leading cholera by 4 to 6 months (Fig. 4). These maps also show coherence with those obtained from correlations of the climate anomaly fields with an ENSO index, instead of cholera, and for a positive lag of 6 months [(21) and figure 3 in (17)]. Thus, the same changes in the atmospheric circulation in south Asia that trail the warming of the Pacific appear to anticipate changes in the interannual variation of cholera in Bangladesh. The time lags in these associations are consistent with the 11-month delay found between cholera and ENSO in our time series analysis.

The above results suggest that an increase in local temperature ultimately mediates the influence of ENSO on cholera. Higher ambient temperatures would correspond to higher water temperatures in shallow bodies of water, such as ponds and rivers in the large estuary of Bangladesh and shallow coastal waters of the Bay of Bengal. Satellite data show that a positive association between

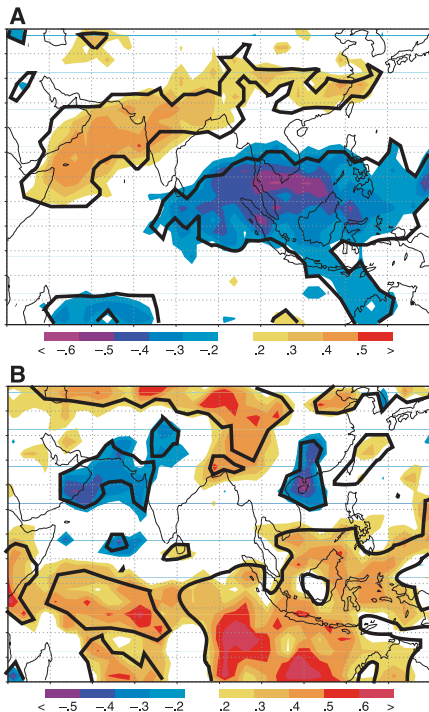


Fig. 4. Maps of correlation coefficients between cholera in Dhaka and anomalies in two satellite-retrieved fields 4 months earlier: (A) upper tropospheric humidity and (B) top-of-atmosphere absorbed solar radiation. The colored regions indicate areas of positive and negative correlations, and the black boundaries indicate the areas where correlations are significant at the 0.002 level. (For each particular point in the map, the significance was calculated with a Monte Carlo test by randomly rearranging the elements of each time series at all points in 999 permutations.)

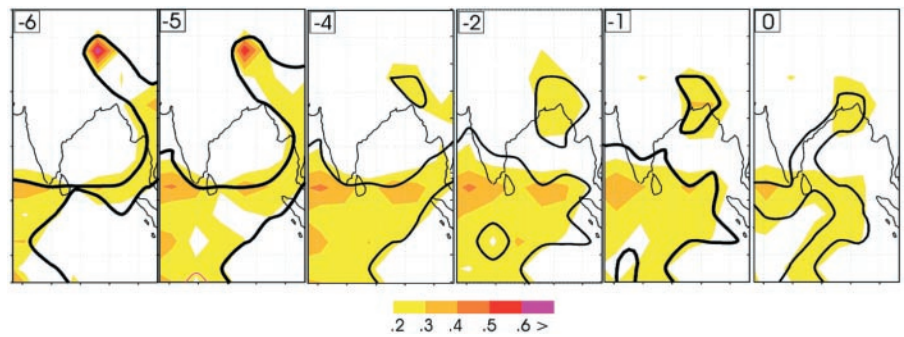


Fig. 5. Maps of correlation coefficients between cholera in Dhaka and temperatures on land and at sea for different lags, with the environmental variable anticipating disease. Monthly temperature data for the period from 1980 to 1995 were extracted from the Global Ocean Surface Temperature Atlas (GOSTAplus) for a grid of 5° latitude and longitude. Data were provided by the NASA Physical Oceanography Distributed Active Archive Center at the Jet Propulsion Laboratory/California Institute of Technology. Black boundaries indicate regions where the correlations are significant at the 0.002 level (see the legend to Fig. 4 for details).

Table 2. Parametric bootstrap test for the significance of additional predictor variables. Comparisons are made only across the best models previously selected with the GVC criterion. The models with previous disease levels and seasonality as the predictor variables are labeled as “dynamic seasonal,” and the model that in addition incorporates the ENSO index is labeled as “seasonal ENSO” ($\tau_f = 11$). The mean, SD, and maximum (Max.) value of Δ_r^2 are computed from the bootstrap data with $n = 1000$. We assess first the significance of adding the ENSO index as a predictor variable by considering the dynamic seasonal models as the null hypothesis. In all cases, the addition of ENSO as a predictor variable is highly significant ($\alpha = 0.001$). We then assess the significance of considering previous disease levels as a predictor variable. We compare the seasonal ENSO model, which does incorporate previous disease levels, to the corresponding model built only from the seasonal clock and the ENSO index, which we label “environmental” ($\tau_f = 11$, $k = 3$). The environmental model performs poorly, with $r^2 = 44\%$ (even for an equal number of neurons k). The addition of previous disease levels as a predictor variable is highly significant ($\alpha = 0.001$). For all comparisons, we also recorded the number of times that the cross-validation criterion failed to select the correct model (the null model). This frequency is given as the probability of ΔV_c being negative in the last column. Results show that this frequency is extremely small for all comparisons.

Null model	Alternative model	Observed $\Delta_0 r^2$	Mean Δ_r^2	SD Δ_r^2	Max. Δ_r^2	Prob. $\Delta V_c < 0$
Dynamic seasonal ($d = 1$)	Seasonal ENSO	12.03	4.90	1.12	10.30	0.03
Dynamic seasonal ($d = 2$)	Seasonal ENSO	9.93	2.00	1.77	7.61	0.024
Environmental	Seasonal ENSO	23.37	1.47	1.18	6.46	0.069

cholera and temperature is first observed to the north of Bangladesh over the Himalayas, where temperature leads cholera increases by 6 months (Fig. 5). The pattern then moves south, though it weakens, as the lag to cholera decreases. Ambient temperatures have also been implicated in the dynamics of diarrhoeal diseases and of *V. cholerae* in the environment in Peru (5, 22), and SSTs have been shown to display a bimodal seasonal cycle similar to that of cholera cases in Bangladesh (2, 4).

Another mediating factor in the ENSO-cholera relation might be the melting of the snowpack in the Himalayas, through its effect on the monsoons, precipitation, and river discharge. This scenario, which remains to be investigated, is suggested by the strong but reduced pattern appearing to the north of Bangladesh (Fig. 5, first and second panels). Floods and droughts can affect not only human interactions with water resources and therefore exposure to the pathogen, but also sanitary conditions and susceptibility to disease.

References and Notes

1. For example, see J. L. Bryden, *Epidemic Cholera in the Bengal Presidency* (Office of the Superintendent of Government Printing, Calcutta, India, 1871).
2. R. R. Colwell, *Science* **274**, 2025 (1996).
3. P. R. Epstein, T. E. Ford, R. R. Colwell, *Lancet* **342**, 1216 (1993).
4. B. Lobitz et al., *Proc. Natl. Acad. Sci. U.S.A.* **97**, 1438 (2000).
5. W. Checkley et al., *Lancet* **355**, 442 (2000).
6. E. Salazar-Lindo, P. Pinell-Salles, A. Maruy, E. Chea-Woo, *Lancet* **350**, 1597 (1997).
7. D. S. Broomhead and G. P. King, *Physica D* **20**, 217 (1986).
8. R. Vautard and M. Ghil, *Physica D* **35**, 395 (1989).
9. Examples of such responses to seasonal forcing in nonlinear models for disease dynamics can be found in W. M. Schaffer et al., in *The Ubiquity of Chaos*, S. Krasner, Ed. (American Association for the Advancement of Science, Washington, DC, 1990), pp. 138–166; I. B. Schwartz and H. L. Smith, *J. Math. Biol.* **18**, 233 (1983); and I. B. Schwartz, *J. Math. Biol.* **30**, 473 (1992).
10. S. Ellner and P. Turchin, *Am. Nat.* **145**, 343 (1995).
11. D. W. Nychka, S. Ellner, A. R. Gallant, D. McCaffrey, *J. R. Stat. Soc. B* **54**, 399 (1992).
12. F. Takens, in *Dynamical Systems and Turbulence*, D. Rand and L. S. Young, Eds., *Lecture Notes in Mathematics*, vol. 898 (Springer-Verlag, New York, 1981), pp. 366–381.
13. M. Casdagli, in *Nonlinear Modeling and Forecasting*, M. Casdagli and S. Eubank, Eds. (Addison-Wesley, New York, 1992).
14. To fit *f* we used the feedforward neural network (FNN) model

$$f(x_1, x_2, \dots, x_d) = \beta_0 + \sum_{i=1}^k \beta_i G \left(\sum_{j=1}^d \gamma_{ij} x_j + \mu_i \right) \quad (2)$$

where *G* is a sigmoid function such as $G(y) = e^y / (1 + e^y)$. Given *k* and the set of independent variables (x_1, x_2, \dots, x_d) , the model parameters $(\beta_0, \beta_i, \gamma_{ij}, \mu_i)$ were estimated by ordinary least squares. Models with different values of *k* or a different set of *x*'s were compared with a GCV criterion function

$$V_c = \left(\frac{RMS}{1 - p/n} \right)^2 \quad (3)$$

where *p* is the number of fitted parameters, and *n* is the sample size. V_1 is the standard GCV criterion [see G. Wahba, *Spline Models for Observational Data* (Society for Industrial and Applied Mathematics, Philadelphia, 1990)]. We used $c = 2$ based on (11). This slight over-penalization of model complexity creates a small bias toward simpler models but greatly reduces the chances of spuriously selecting an overly complex model. The FNN models were fitted with FUNFITS, a suite of S/Fortran functions that run in S-Plus (see www.cgd.ucar.edu/stats/Funfits/).

15. We evaluate the significance of the improvement in fit between a "full" model that incorporates a predictor variable and a "reduced" model that omits the variable. The bootstrap test procedure consists of generating a large number of artificial time series with the reduced model and fitting each of these time series with both the full and reduced models. The artificial time series are generated from the reduced model by adding a vector of randomized residuals to the vector of predictions from the reduced model. In the few cases where the resulting values are negative, we replace them by a lower threshold of 0.1 (equal to the minimum value observed in the data). The improvement in fit between the full and reduced models on the original data is compared to the improvements in fit on the artificial time series, in which any apparent improvement is an artifact of the larger number of parameters and variables in the full model. Let $\Delta_i r^2$ denote the difference in r^2 between the full and reduced models for the *i*th time series (with *i* = 0 being the original data and *i* = 1, 2, ... *n* being the artificial data). Let p be the fraction of $\Delta_i r^2, i > 0$ values that are larger than $\Delta_0 r^2$. The reduced model is then rejected in favor of the full model at significance level α if $p < \alpha$.

16. See, for example, B. Finkenstädt, M. Keeling, B. T. Grenfell, *Proc. R. Soc. London Ser. B* **265**, 753 (1998).
17. S. A. Klein, B. J. Soden, N. Lau, *J. Clim.* **12**, 917 (1999).
18. Monthly measurements of upper-tropospheric humidity for the period 1979–92 [J. Schmetz, L. Vanderberg, C. Geijo, K. Holmlund, *Adv. Space Res.* **16**, 69 (1995); B. J. Soden and F. P. Bretherton, *J. Geophys. Res.* **101**, 9333 (1996)].
19. Monthly measurements of cloud cover for the period 1983–91 are from the International Satellite Cloud Climatology Project [W. B. Rossow and R. A. Schiffer, *Bull. Am. Meteorol. Soc.* **72**, 2 (1991)].
20. Monthly measurements of top-of-atmosphere absorbed solar radiation for the period 1985–89 are from the Earth Radiation Budget Experiment [E. F. Harrison et al., *J. Geophys. Res.* **95**, 18687 (1990)].
21. A supplementary figure is available at Science Online at www.sciencemag.org/feature/data/1051490.shl.
22. A. A. Franco et al., *Am. J. Epidemiol.* **146**, 1067 (1997).
23. M. Ghil and K. Mo, *J. Atmos. Sci.* **48**, 752 (1991).
24. ———, *J. Atmos. Sci.* **48**, 780 (1991).
25. We thank K. Siddique and G. Fuchs for assistance with the cholera data; R. B. Sack, J. Trantj, and the Office of Global Programs at the National Oceanic and Atmospheric Administration for stimulating this work; B. Soden for the cloud cover and radiation data; and M. A. Rodriguez-Arias for computing assistance. M.P. was supported by a James S. McDonnell Foundation Centennial Fellowship and by The Knut and Alice Wallenbergs Foundation; S.P.E. was supported by a grant from the Mellon Foundation to S.P.E. and N.G. Hairston Jr.; X.R. received partial support from the Commissionat per Universitats i Recerca.

19 April 2000; accepted 6 July 2000

Myotonic Dystrophy in Transgenic Mice Expressing an Expanded CUG Repeat

Ami Mankodi,¹ Eric Logigian,¹ Linda Callahan,² Carolyn McClain,¹ Robert White,¹ Don Henderson,¹ Matt Krym,¹ Charles A. Thornton^{1*}

Myotonic dystrophy (DM), the most common form of muscular dystrophy in adult humans, results from expansion of a CTG repeat in the 3' untranslated region of the *DMPK* gene. The mutant *DMPK* messenger RNA (mRNA) contains an expanded CUG repeat and is retained in the nucleus. We have expressed an untranslated CUG repeat in an unrelated mRNA in transgenic mice. Mice that expressed expanded CUG repeats developed myotonia and myopathy, whereas mice expressing a nonexpanded repeat did not. Thus, transcripts with expanded CUG repeats are sufficient to generate a DM phenotype. This result supports a role for RNA gain of function in disease pathogenesis.

Myotonic dystrophy (DM, prevalence 1 in 7400 live births) is characterized by dominantly inherited muscle hyperexcitability (myotonia), progressive myopathy, cataracts, defects of cardiac conduction, neuropsychiatric impairment, and other developmental and degenerative manifestations (1). This complex phenotype re-

sults from the expansion of a CTG repeat in the 3' untranslated region (3'UTR) of the *DMPK* gene, which encodes a serine-threonine protein kinase (2). The transcripts from the mutant allele are retained in the nucleus (3, 4), and levels of *DMPK* protein are correspondingly reduced (5). The expanded repeat also changes the structure of adjacent chromatin (6) and silences the expression of a flanking gene (7, 8), *SIX5*, which encodes a transcription factor.

The effects on *DMPK* and *SIX5* expression may account for particular aspects of the DM phenotype. *Dmpk* knockout mice have reduced force generation in skeletal muscle (9) and ab-

¹Department of Neurology, ²Department of Neurobiology and Anatomy, School of Medicine and Dentistry, University of Rochester, Box 673, 601 Elmwood Avenue, Rochester, NY 14642, USA.

*To whom correspondence should be addressed. E-mail: charles_thornton@urmc.rochester.edu